



# Two-dimensional g-C<sub>3</sub>N<sub>4</sub>/Ca<sub>2</sub>Nb<sub>2</sub>TaO<sub>10</sub> nanosheet composites for efficient visible light photocatalytic hydrogen evolution

Supphasin Thaweesak, Miaoqiang Lyu, Piangjai Peerakiatkhajohn, Teera Butburee, Bin Luo, Hongjun Chen, Lianzhou Wang\*

Nanomaterials Centre, School of Chemical Engineering and Australian Institute for Bioengineering and Nanotechnology, The University of Queensland, St Lucia QLD 4072, Australia

## ARTICLE INFO

### Article history:

Received 15 March 2016

Received in revised form 5 September 2016

Accepted 12 September 2016

Available online 12 September 2016

### Keywords:

Photocatalysis

g-C<sub>3</sub>N<sub>4</sub> nanosheets

Ca<sub>2</sub>Nb<sub>2</sub>TaO<sub>10</sub> nanosheets

Composites

H<sub>2</sub> production

## ABSTRACT

Scalable g-C<sub>3</sub>N<sub>4</sub> nanosheet powder catalyst was prepared by pyrolysis of dicyandiamide and ammonium chloride followed by ultra-sonication and freeze-drying. Nanosheet composite that combines the g-C<sub>3</sub>N<sub>4</sub> nanosheets and Ca<sub>2</sub>Nb<sub>2</sub>TaO<sub>10</sub> nanosheets with various ratios were developed and applied as photocatalysts for solar hydrogen generation. Systematic studies reveal that the g-C<sub>3</sub>N<sub>4</sub>/Ca<sub>2</sub>Nb<sub>2</sub>TaO<sub>10</sub> nanosheet composite with a mass ratio of 80:20 shows the best performance in photocatalytic H<sub>2</sub> evolution under visible light-irradiation, which is more than 2.8 times out-performing bare g-C<sub>3</sub>N<sub>4</sub> bulk. The resulting nanosheets possess a high surface area of 96 m<sup>2</sup>/g, which provides abundance active sites for the photocatalytic activity. More importantly, the g-C<sub>3</sub>N<sub>4</sub>/Ca<sub>2</sub>Nb<sub>2</sub>TaO<sub>10</sub> nanosheet composite shows efficient charge transfer kinetics at its interface, as evident by the photoluminescence measurement. The intimate interfacial connections and the synergistic effect between g-C<sub>3</sub>N<sub>4</sub> nanosheets and Ca<sub>2</sub>Nb<sub>2</sub>TaO<sub>10</sub> nanosheets with cascading electrons are efficient in suppressing charge recombination and improving photocatalytic H<sub>2</sub> evolution performance.

© 2016 Elsevier B.V. All rights reserved.

## 1. Introduction

Over the past two decades, sustainable energy has become a great interest to address the global energy crisis and environmental pollution. The development of technologies that enable to use renewable energy source such as solar energy has been driven by semiconductor in photocatalytic water splitting, which involves the conversion of solar energy and water into chemical energy stored by hydrogen. To design photocatalytic water splitting system the semiconductor photocatalyst mainly requires high efficiency, stability, capability to harvest light in the visible spectrum, environmentally benign, and inexpensive [1,2]. However, there are many issues needed to be solved in order to meet the demanding photocatalytic performance, such as limited visible-light response and high recombination rate of photogenerated electron-hole pairs [3].

Hybridization between different photocatalyst materials attracts a great interest to overcome the limitation of a conventional single-photocatalyst design [4,5]. The synergistic coupling

is effective in optimizing their performance and even creating unexpected functionality for practical applications [6,7]. Since the chemical interactions between each kind of chemical species are important to realize the benefit of hybridization, hence an expanded surface area nanostructures becomes anticipated for fabricating functional hybrid materials [8,9]. Graphitic carbon nitride (g-C<sub>3</sub>N<sub>4</sub>), a typical layered structure, has been studied in various areas such as CO<sub>2</sub> reduction [10], degradation of organic pollutant [3,11], photocatalytic water splitting [4,12]. g-C<sub>3</sub>N<sub>4</sub> is attractive because of its suitable band gap for visible light absorption, band edge positions straddle water splitting redox potential, and good chemical and thermal stability. Nevertheless, the efficiency is unsatisfactory and hampers its practical application due to high recombination rate of photogenerated electron-hole pairs. Therefore, several strategies have been developed, including the construction of a porous structure [13], doping with nonmetal elements [14], modification with carbon material [15], and coupling with other semiconductors to form hybridized composites [16].

Niobium phase layered perovskite Dion-Jacobson compounds have a general chemical formula A<sub>x</sub>[B<sub>n-1</sub>Nb<sub>n</sub>O<sub>3n+1</sub>], where A represents an alkaline ion K<sup>+</sup>, Rb<sup>+</sup>, Cs<sup>+</sup>; B represents an alkaline earth ion Ca<sup>2+</sup>, Sr<sup>2+</sup>, lead, bismuth, lanthanides, and n represents NbO<sub>6</sub> octahedral perovskite-like slab stacking along the (001)

\* Corresponding author.

E-mail address: [l.wang@uq.edu.au](mailto:l.wang@uq.edu.au) (L. Wang).

direction to form a three-dimensional crystal. Recently, Dion-Jacobson phase  $\text{Ca}_2\text{Nb}_2\text{TaO}_{10}$  was reported to exhibit the good photocatalytic activity of restacked nanosheet for  $\text{H}_2$  evolution from an aqueous methanol solution under ultraviolet irradiation [17]. However, to date there is no report focusing on the composite photocatalyst design by rationally combining two types of  $\text{g-C}_3\text{N}_4$  and  $\text{Ca}_2\text{Nb}_2\text{TaO}_{10}$  nanosheets. In this study, we report the hybridization of these two types of two-dimensional nanostructured materials for an efficient hybrid photocatalyst via a facile solution exfoliation-reassembly process. The resultant materials exhibited remarkably improved  $\text{H}_2$  evolution performance under visible light. The crystal structure and morphology of the nanocomposites were investigated systematically and the photocatalytic activity of the nanocomposites for  $\text{H}_2$  evolution was discussed in details.

## 2. Experimental section

### 2.1. Catalyst preparation

The  $\text{g-C}_3\text{N}_4$  bulk was prepared by thermal condensation of dicyandiamide according to a reported method [4]. In a typical synthesis, dicyandiamide precursor was placed in an alumina crucible and thermally heated in a muffle furnace at  $550^\circ\text{C}$  for 4 h. The obtained yellow agglomerate product was collected and ground into a powder for further use.

As for the synthesis of  $\text{g-C}_3\text{N}_4$  nanosheet, it was prepared according to a reported method [18] with some modification. 1 g of dicyandiamide was firstly mixed with 10 g of ammonium chloride and ground in a mortar for 30 min. The obtained mixture was transferred into an alumina crucible and thermally treated in a muffle furnace at  $550^\circ\text{C}$  for 4 h, resulting in a pale yellow sponge-like product. Subsequently, 0.3 g of the product was ground and immersed in 100 ml, Milli-Q water then treated under ultrasonication for 1 h. After the ultrasonication was completed, the nanosheet product was centrifuge at 3000 rpm for 5 min. The supernatant was separated from unexfoliated  $\text{g-C}_3\text{N}_4$ , and  $\text{g-C}_3\text{N}_4$  nanosheets with a concentration of ca. 0.7 g/L were obtained.

For the preparation of  $\text{Ca}_2\text{Nb}_2\text{TaO}_{10}$  nanosheet, firstly layered  $\text{KCa}_2\text{Nb}_2\text{TaO}_{10}$  was synthesized by the polymerized complex method then followed by proton exchange and exfoliation according to the method reported by in literature [17,19,20]. In a typical synthesis, 4.15 g of  $\text{NbCl}_5$  and 2.75 g of  $\text{TaCl}_5$  and 36.02 g of anhydrous citric acid powder was dissolved in 117 ml of methanol with vigorous stirring. After complete dissolution was achieved, 18.01 g of  $\text{CaCO}_3$ , 0.63 g of KCl and 58 g of ethylene glycol were added to the solution. The solution mixture was heated on a hot plate with stirring in a fume cupboard to  $100^\circ\text{C}$  to promote dissolution. Then, the as-obtained transparent solution was heated to  $130^\circ\text{C}$  with continuous stirring for methanol evaporation. After 30 min of continuous stirring, the temperature is increased to  $200^\circ\text{C}$  and kept stirring for several hours to promote polymerization and to remove excess ethylene glycol until the solution became highly viscous and its color turn from clear transparent to brown transparent. The resin was pyrolyzed in air at  $375^\circ\text{C}$  for 4 h resulted in a black power. Then, the black powder was ground and placed on an alumina plate then heated at  $650^\circ\text{C}$  for 4 h in static air. The as-obtained powder was further calcined at  $1000^\circ\text{C}$  for 2 h in an alumina crucible at a ramping rate  $10^\circ\text{C}/\text{min}$ . The resulting powder 5 g was stirred in 200 ml of aqueous nitric acid (1 M) at room temperature (the fresh aqueous nitric acid was replaced every 24 h) for 1 week. The proton-exchanged product was isolated by centrifugation, washed with copious water to remove acid residue and finally air-dried overnight. Finally, the proton-exchanged powder was mixed with aqueous tetra(*n*-butyl)ammonium hydroxide (Aldrich chemi-

cal Co., 40 wt.% in  $\text{H}_2\text{O}$ ) and shaken at room temperature for 1 week. The nanosheet product was centrifuged at 3000 rpm for 5 min. The supernatant was separated from unexfoliated  $\text{Ca}_2\text{Nb}_2\text{TaO}_{10}$ , to obtain the exfoliated  $\text{Ca}_2\text{Nb}_2\text{TaO}_{10}$  nanosheets (concentration: 2.39 g/).

The typical preparation of  $\text{g-C}_3\text{N}_4/\text{Ca}_2\text{Nb}_2\text{TaO}_{10}$  nanosheet composite photocatalysts was as follows [21]: The pH of  $\text{Ca}_2\text{Nb}_2\text{TaO}_{10}$  nanosheets suspension was adjusted to be 9–11 by diluted tetrabutylammonium hydroxide solution. The polyethylenimine (PEI,  $\text{Mw} = 7.5 \times 10^5$  g) solution with a concentration of 50 g/L and pH 9–11 (5 ml) was slowly added into  $\text{Ca}_2\text{Nb}_2\text{TaO}_{10}$  solution. The mixture  $\text{Ca}_2\text{Nb}_2\text{TaO}_{10}$  nanosheet suspension was stirred 2 h then  $\text{g-C}_3\text{N}_4$  was added to the mixture and stirred overnight. The  $\text{g-C}_3\text{N}_4/\text{Ca}_2\text{Nb}_2\text{TaO}_{10}$  nanosheet composite was centrifuge at 20,000 rpm, the precipitated was freeze-dried. The dried composite powder was added into a crucible and then heated in a muffle furnace at  $400^\circ\text{C}$ , for 1 h with a heating rate of  $1^\circ\text{C}/\text{min}$ . The final  $\text{g-C}_3\text{N}_4/\text{Ca}_2\text{Nb}_2\text{TaO}_{10}$  nanosheet photocatalysts were obtained. For the preparation of  $\text{g-C}_3\text{N}_4/\text{Ca}_2\text{Nb}_2\text{TaO}_{10}$  bulk, the  $\text{g-C}_3\text{N}_4$  bulk and  $\text{Ca}_2\text{Nb}_2\text{TaO}_{10}$  bulk was mixed in a mortar for 15 min. the as-obtained mixture was calcined in a muffle furnace at  $400^\circ\text{C}$ , for 1 h with a heating rate of  $1^\circ\text{C}/\text{min}$ . The final  $\text{g-C}_3\text{N}_4/\text{Ca}_2\text{Nb}_2\text{TaO}_{10}$  bulk composite photocatalysts were obtained.

### 2.2. Sample characterization

The synthesized samples crystallinity was characterized by X-ray diffractometer (Bruker Advanced, 40 kV and 30 mA) with  $\text{Cu K}\alpha$  radiation. The diffuse reflectance spectra were conducted using UV-vis spectrometer (V-650, Jasco) equipped with an integrating sphere in the range of 300–800 nm. The chemical characterization was obtained by X-ray photoelectron spectroscopy (XPS, Thermo Escalab 250, a monochromatic Axis ULTRA X-ray). The surface morphology was analyzed by field-emission scanning electron microscopy (FESEM; JSM7100, JEOL, Tokyo, Japan), transmission electron microscopy (TEM; JEOL 1010, Tokyo, Japan) and a high resolution transmission electron microscopy (HRTEM, JEM-2100F, JEOL, Tokyo, Japan). The amount of  $\text{H}_2$  evolved from the photocatalyst samples inside the photocatalytic reactor was measured by a gas chromatography (Shimadzu, GC-2014). The surface charge was measured by Zetasizer (Nano-ZS) from Malvern Instruments. The surface area measurement of the solid material was analyzed by Micromeritics TriStar 3000.

### 2.3. Photocatalytic hydrogen evolution test

The photocatalytic  $\text{H}_2$  evolution reactions were carried out in a quartz top irradiation reactor connected with gas chromatography (Shimadzu, GC-2014) equipped with a thermal conductive detector (TCD) and a  $5\text{A}^\circ$  molecular sieve column, with Argon as the carrier gas. The temperature of the reactor was maintained at  $0^\circ\text{C}$  by a jacket with the flow of cooling water during the photocatalytic reaction. A 300 W Xenon arc lamp with an output power of 19 A was used as light source. In a typical reaction, 50 mg photocatalyst was suspended in 200 ml aqueous solution containing triethanolamine 10 vol%, and  $\text{H}_2\text{PtCl}_6$  solution equivalent to 1 wt% Pt was added into a glass reactor. Prior to the photocatalytic reaction experiment, the reactor system was vacuumed several times to remove gasses. The reactor was illuminated for 30 min by in situ photodeposition for loading Pt co-catalyst on photocatalyst surface by with a 300 W Xe lamp equipped with a 400 nm cut-off filter.

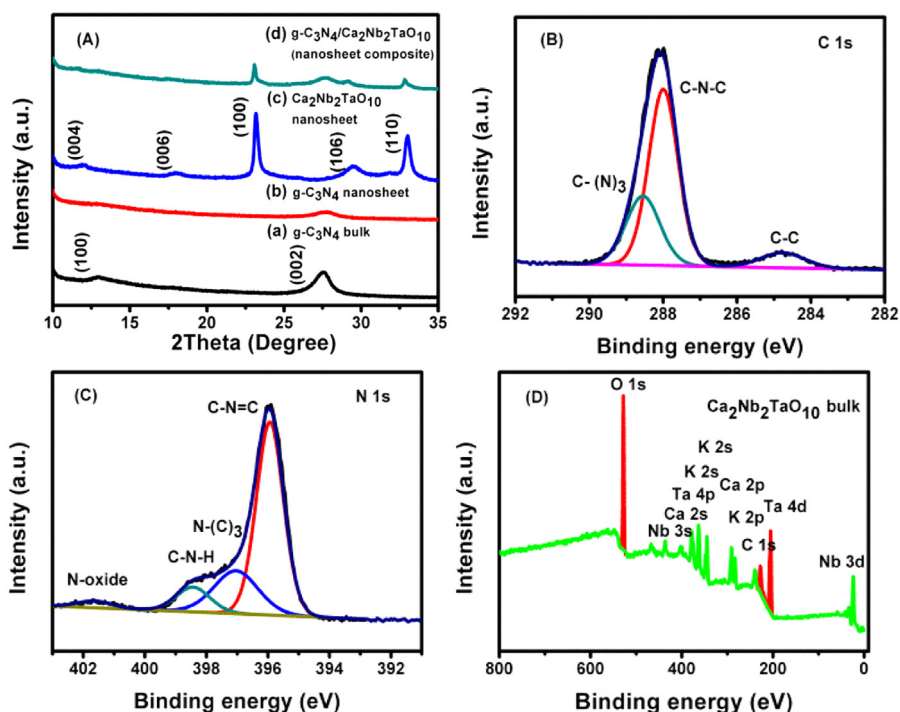


**Fig. 1.** (A) XRD patterns of (a) g-C<sub>3</sub>N<sub>4</sub> bulk, (b) g-C<sub>3</sub>N<sub>4</sub> nanosheets, (c) Ca<sub>2</sub>Nb<sub>2</sub>TaO<sub>10</sub> nanosheets and (d) g-C<sub>3</sub>N<sub>4</sub>/Ca<sub>2</sub>Nb<sub>2</sub>TaO<sub>10</sub> composite nanosheets. (B) High-resolution XPS spectra of C 1s and (C) N 1s, and (D) survey XPS spectra of Ca<sub>2</sub>Nb<sub>2</sub>TaO<sub>10</sub> bulk materials.

### 3. Results and discussion

#### 3.1. Characterization of photocatalysts

The powder XRD patterns were conducted to identify the formation of the g-C<sub>3</sub>N<sub>4</sub> bulk, g-C<sub>3</sub>N<sub>4</sub> nanosheets, Ca<sub>2</sub>Nb<sub>2</sub>TaO<sub>10</sub> nanosheets and g-C<sub>3</sub>N<sub>4</sub>/Ca<sub>2</sub>Nb<sub>2</sub>TaO<sub>10</sub> composite with a mass ratio of 80:20. In Fig. 1A(a, b), the XRD pattern of g-C<sub>3</sub>N<sub>4</sub> bulk and g-C<sub>3</sub>N<sub>4</sub> nanosheets reveal a distinct peak at about 27° and a weak peak about 13.1° which could be indexed as (002) and (100) diffraction planes corresponding to the inter-planar stacking peak of aromatic system and the lattice plane structural packing to the c-axis, respectively [10,22]. The intensity of the diffraction (002) and (100) plane of g-C<sub>3</sub>N<sub>4</sub> nanosheets significantly decreases, and diffraction plane (002) slightly shifts from 27.7° to 28° compared to g-C<sub>3</sub>N<sub>4</sub> bulk. These clearly confirm the decrease of the planar size of the g-C<sub>3</sub>N<sub>4</sub> layers during exfoliation and successful preparation of the two-dimensional g-C<sub>3</sub>N<sub>4</sub> nanosheets [18,22,23]. In Fig. 1A(c), the XRD pattern of restacked Ca<sub>2</sub>Nb<sub>2</sub>TaO<sub>10</sub> nanosheets sample reveals two distinct diffraction peaks at about 23.2° and 33.0° and three weak diffraction peaks. The two distinct diffraction peaks can be indexed as (100) and (110) diffraction planes which are related to the in-plane diffraction, indicating the two-dimensional feature of restacked nanosheets [17,24]. In Fig. 1A(d), the XRD pattern of g-C<sub>3</sub>N<sub>4</sub>/Ca<sub>2</sub>Nb<sub>2</sub>TaO<sub>10</sub> nanosheet composite shows weak diffraction peaks at about 23.0°, 27.6°, 29.1°, and 32.8°. The diffraction peak at 27.6° can be indexed as the diffraction peak of g-C<sub>3</sub>N<sub>4</sub> nanosheets (Fig. 1A(b)) and the other 23.0°, 29.1°, and 32.8° are in agreement with the characteristics of Ca<sub>2</sub>Nb<sub>2</sub>TaO<sub>10</sub> nanosheets (Fig. 1A(c)). The XRD pattern of g-C<sub>3</sub>N<sub>4</sub>/Ca<sub>2</sub>Nb<sub>2</sub>TaO<sub>10</sub> nanosheet composite reveals the coexistence of Ca<sub>2</sub>Nb<sub>2</sub>TaO<sub>10</sub> and g-C<sub>3</sub>N<sub>4</sub> in the composite. The X-ray photoelectron spectroscopy (XPS) analysis was conducted to investigate the chemical composition state of g-C<sub>3</sub>N<sub>4</sub> bulk and Ca<sub>2</sub>Nb<sub>2</sub>TaO<sub>10</sub> bulk. The high resolution of C 1s XPS spectra in Fig. 1B displays the sp<sup>2</sup> C atoms bonded to N in the sample as C-(N)<sub>3</sub> (288.5 eV) and C-N-C (287.9 eV) and adven-

titious carbon (C-C) (284.7 eV) [18,25]. The high resolution of N 1s XPS spectra in Fig. 1C, displays typical triazine rings repeating unit of sp<sup>2</sup> hybridized nitrogen with different N bonding including, the dominant N of pyridinic bridging N atoms in nitrogen C=N=C (395.94 eV), tertiary nitrogen N-(C)<sub>3</sub> (397.08 eV) and terminal amino group C-N-H (398.45 eV) [26,27]. The very weak N spectra at 401.58 eV can be assigned to N-oxide or the charging effects in the cyano group and heterocycles or positive charge localization [9]. The survey XPS spectra in Fig. 1D reveals chemical elements, Ca 2s, Ca 2p, Nb 3s, Nb 3d, Ta 4p, Ta 4d, O 1s on the surface of Ca<sub>2</sub>Nb<sub>2</sub>TaO<sub>10</sub>, confirming the chemical elements of synthesized Ca<sub>2</sub>Nb<sub>2</sub>TaO<sub>10</sub> nanosheet.

The optical absorption properties of the g-C<sub>3</sub>N<sub>4</sub> bulk, g-C<sub>3</sub>N<sub>4</sub> nanosheet, Ca<sub>2</sub>Nb<sub>2</sub>TaO<sub>10</sub> nanosheets, and g-C<sub>3</sub>N<sub>4</sub>/Ca<sub>2</sub>Nb<sub>2</sub>TaO<sub>10</sub> bulk and nanosheet composite were investigated by UV/Vis diffuse reflectance spectroscopy, as shown in Fig. 2. It is clear that the g-C<sub>3</sub>N<sub>4</sub> has a visible light absorption characteristic, the absorption onset of the exfoliated g-C<sub>3</sub>N<sub>4</sub> nanosheets (447 nm) exhibits a slight blue shift in comparison with the g-C<sub>3</sub>N<sub>4</sub> bulk (467 nm) due to the quantum size effect [26]. Note that the bare sample of restacked Ca<sub>2</sub>Nb<sub>2</sub>TaO<sub>10</sub> nanosheets exhibits a UV light absorption peak with the absorption onset located at approximately 337 nm [17] and a relatively broad visible light absorption tail. The visible light absorption of Ca<sub>2</sub>Nb<sub>2</sub>TaO<sub>10</sub> nanosheets may arise from incorporation of some organic chemical tetrabutylammonium (TBA<sup>+</sup>) during the restacking process. Upon the calcination, a trace amount of carbon residue may causes to the broad visible light absorption [28,29]. In contrast, the g-C<sub>3</sub>N<sub>4</sub>/Ca<sub>2</sub>Nb<sub>2</sub>TaO<sub>10</sub> nanosheet composite sample shows much sharper absorption onset in the visible region, suggesting that g-C<sub>3</sub>N<sub>4</sub>/Ca<sub>2</sub>Nb<sub>2</sub>TaO<sub>10</sub> nanosheet composite may have potential application as a visible light photocatalyst.

The morphologies and microstructure of the g-C<sub>3</sub>N<sub>4</sub> bulk, g-C<sub>3</sub>N<sub>4</sub> nanosheets, and g-C<sub>3</sub>N<sub>4</sub>/Ca<sub>2</sub>Nb<sub>2</sub>TaO<sub>10</sub> composites were investigated by scanning electron microscopy (SEM), transmission electron microscopy (TEM). Fig. 3a shows a large aggregated layered particle with several stacking layers of as- prepared g-C<sub>3</sub>N<sub>4</sub>



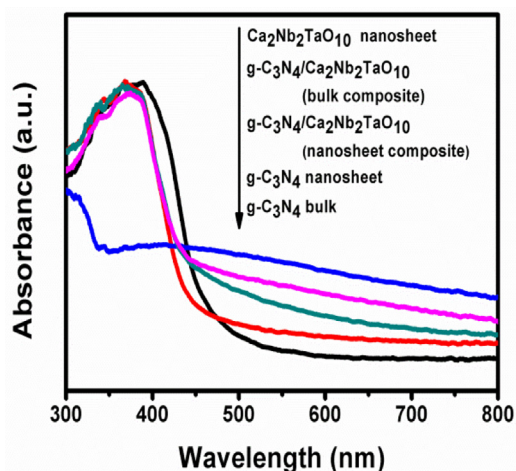


**Fig. 2.** UV/vis diffuse reflection spectra of the samples. Blue:  $\text{Ca}_2\text{Nb}_2\text{TaO}_{10}$  nanosheets, Pink:  $\text{g-C}_3\text{N}_4/\text{Ca}_2\text{Nb}_2\text{TaO}_{10}$  bulk composite, Aqua:  $\text{g-C}_3\text{N}_4/\text{Ca}_2\text{Nb}_2\text{TaO}_{10}$  nanosheet composite, Red:  $\text{g-C}_3\text{N}_4$  nanosheets, Black:  $\text{g-C}_3\text{N}_4$  bulk. (For interpretation of the references to color in this figure legend, the reader is referred to the web version of this article.)

bulk. The SEM of  $\text{g-C}_3\text{N}_4$  nanosheet after exfoliation and freeze-drying shows a crinkly structure (Fig. 3b). The TEM image of  $\text{g-C}_3\text{N}_4$  nanosheet (Fig. 3c) presents the ultra-thin characteristic of the exfoliated nanosheet. The as-prepared  $\text{Ca}_2\text{Nb}_2\text{TaO}_{10}$  sample displays a stacking flat layered structure in Fig. 3d, while the exfoliated and freeze-drying product shows thinner sheet with a lateral size of  $\sim 200$  nm (Fig. 3e, f).

As shown in Fig. 4a, The SEM images of  $\text{g-C}_3\text{N}_4/\text{Ca}_2\text{Nb}_2\text{TaO}_{10}$  reveals that large  $\text{Ca}_2\text{Nb}_2\text{TaO}_{10}$  nanosheets attached to the  $\text{g-C}_3\text{N}_4$  nanosheets, forming a heterostructure of  $\text{g-C}_3\text{N}_4/\text{Ca}_2\text{Nb}_2\text{TaO}_{10}$  nanosheet composite. In comparison, Fig. 4b, the  $\text{g-C}_3\text{N}_4/\text{Ca}_2\text{Nb}_2\text{TaO}_{10}$  bulk composite reveals separated chunks of material with a size of several micrometers. The low and high TEM images of  $\text{g-C}_3\text{N}_4/\text{Ca}_2\text{Nb}_2\text{TaO}_{10}$  nanosheet composite are shown in Fig. 4c and d, respectively. Fig. 4c, the darker rectangular shape nanosheet should be  $\text{Ca}_2\text{Nb}_2\text{TaO}_{10}$  as

revealed from SEM and TEM images of  $\text{Ca}_2\text{Nb}_2\text{TaO}_{10}$  in Fig. 3e and f, respectively, while the lighter part should be  $\text{g-C}_3\text{N}_4$  nanosheets. Further HR-TEM analysis was conducted to confirm the microstructures of  $\text{g-C}_3\text{N}_4/\text{Ca}_2\text{Nb}_2\text{TaO}_{10}$ . From the HR-TEM image of  $\text{g-C}_3\text{N}_4/\text{Ca}_2\text{Nb}_2\text{TaO}_{10}$  composite shown in Fig. 4d, the intimate contact between 2D exfoliated  $\text{g-C}_3\text{N}_4$  and  $\text{Ca}_2\text{Nb}_2\text{TaO}_{10}$  nanosheets can be observed. The less ordered area in the left-hand side of Fig. 4d might be assigned to  $\text{g-C}_3\text{N}_4$  [30], while the better crystalline lattice fringes can be associated with exfoliated  $\text{Ca}_2\text{Nb}_2\text{TaO}_{10}$  nanosheets. The formation of interconnected heterostructure in  $\text{g-C}_3\text{N}_4/\text{Ca}_2\text{Nb}_2\text{TaO}_{10}$  nanosheet composites should be beneficial to the photocatalytic activity of the materials, as will be discussed in the following sections.

### 3.2. Photocatalytic $\text{H}_2$ evolution

The photocatalytic  $\text{H}_2$  evolution experiments were carried out to evaluate the performance of the pristine  $\text{g-C}_3\text{N}_4$  nanosheets,  $\text{Ca}_2\text{Nb}_2\text{TaO}_{10}$  nanosheets, and  $\text{g-C}_3\text{N}_4/\text{Ca}_2\text{Nb}_2\text{TaO}_{10}$  nanosheet composites photocatalysts. In the control experiments, we first examined the effects of illumination on triethanolamine (TEOA) aqueous solution in the absence of a photocatalyst, and the role of Pt co-catalyst on  $\text{g-C}_3\text{N}_4$  bulk sample. The result reveals that there is no  $\text{H}_2$  evolution occurred in the absence of a catalyst and negligible amount of  $\text{H}_2$  evolution from  $\text{g-C}_3\text{N}_4$  bulk in the absence of Pt co-catalyst. Fig. 5A presents the  $\text{H}_2$  evolution rates of all samples tested under visible light irradiation. During 4 h of irradiation, the rate of  $\text{H}_2$  Evolution over  $\text{g-C}_3\text{N}_4$  bulk (Fig. 5A,a) can produce  $\text{H}_2$  at a rate of  $15.1 \mu\text{mol/h}$ . Upon modifying the  $\text{g-C}_3\text{N}_4$  bulk by exfoliation into  $\text{g-C}_3\text{N}_4$  nanosheets, the photocatalytic performance of the  $\text{g-C}_3\text{N}_4$  nanosheets (Fig. 5A,b) was further increased to  $31.29 \mu\text{mol/h}$ , which is about 2 times higher than  $\text{g-C}_3\text{N}_4$  bulk. It is interesting to investigate the possible reasons for improved photocatalytic performance in the composite photocatalysts. The specific surface area of the  $\text{g-C}_3\text{N}_4$  nanosheets was  $43.81 \text{ m}^2/\text{g}$ , which was higher than  $\text{g-C}_3\text{N}_4$  bulk ( $7.56 \text{ m}^2/\text{g}$ ) [27], however the photocatalytic performance not proportionally increased with larger surface areas, suggesting the surface area is not the only reason for photocatalytic property. As shown in Fig. 2,

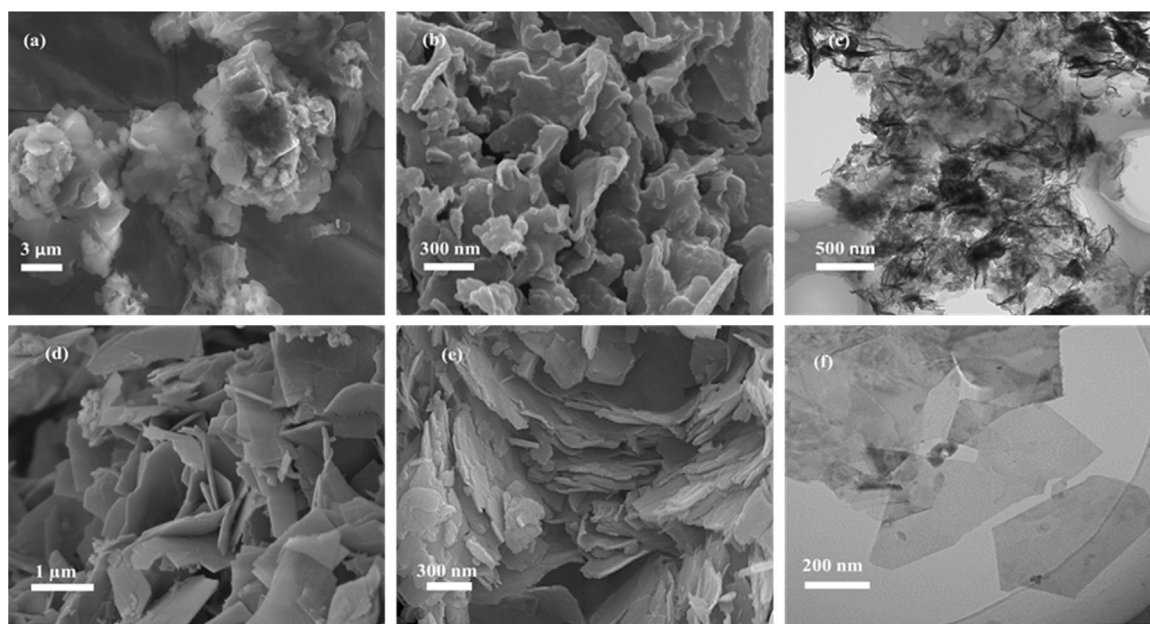


**Fig. 3.** SEM images of (a)  $\text{g-C}_3\text{N}_4$  bulk, (b)  $\text{g-C}_3\text{N}_4$  nanosheets, (d)  $\text{Ca}_2\text{Nb}_2\text{TaO}_{10}$  bulk, and (e)  $\text{Ca}_2\text{Nb}_2\text{TaO}_{10}$  nanosheets. TEM images of (c)  $\text{g-C}_3\text{N}_4$  nanosheets, and (f)  $\text{Ca}_2\text{Nb}_2\text{TaO}_{10}$  nanosheets.

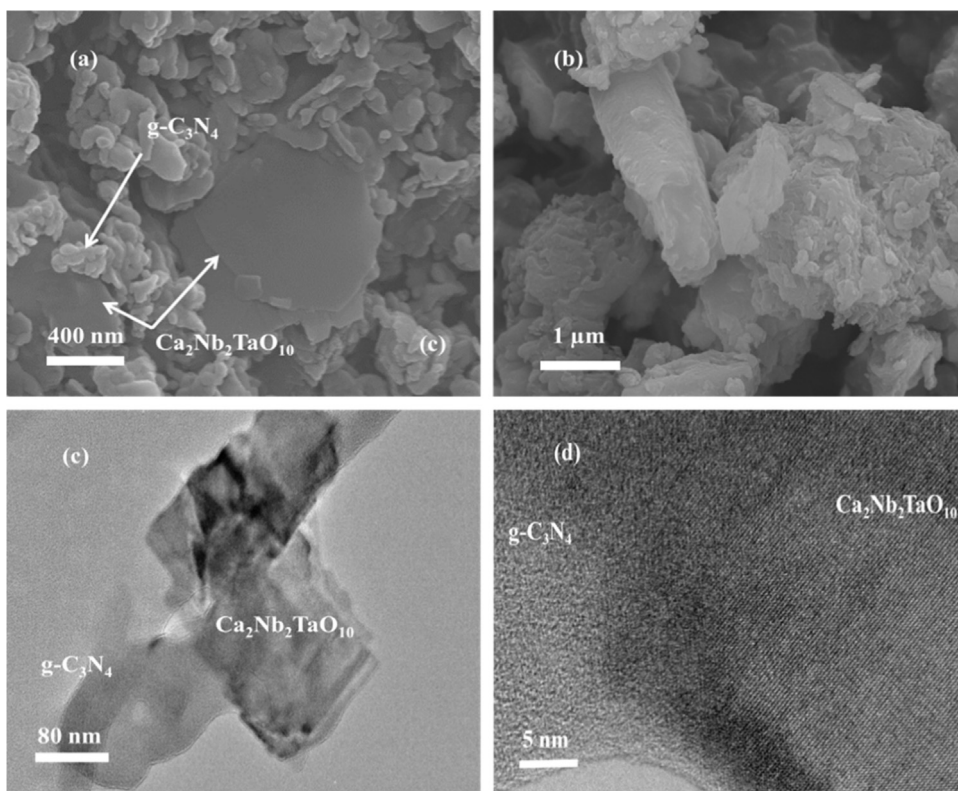


**Fig. 4.** a) SEM image of  $g\text{-C}_3\text{N}_4/\text{Ca}_2\text{Nb}_2\text{TaO}_{10}$  nanosheet composite, b) SEM image of  $g\text{-C}_3\text{N}_4/\text{Ca}_2\text{Nb}_2\text{TaO}_{10}$  bulk, c) Low, and d) High Resolution TEM image of  $g\text{-C}_3\text{N}_4/\text{Ca}_2\text{Nb}_2\text{TaO}_{10}$  composite nanosheets.

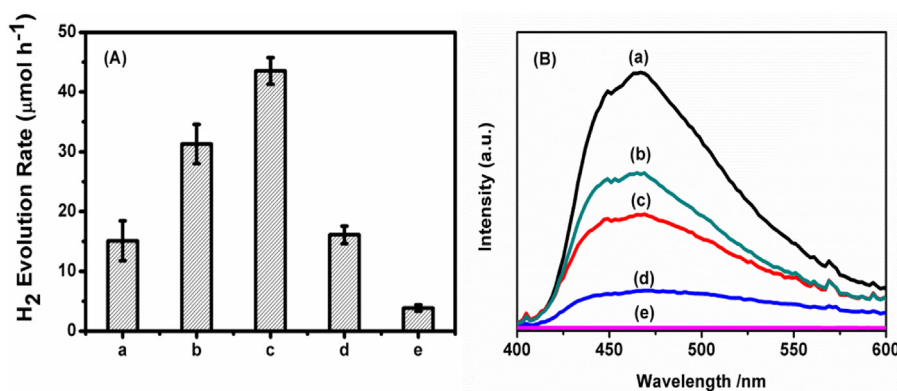


**Fig. 5.** (A) Photocatalytic  $\text{H}_2$  evolution rates on the photocatalyst samples: (a)  $g\text{-C}_3\text{N}_4$  bulk, (b)  $g\text{-C}_3\text{N}_4$  nanosheets, (c)  $g\text{-C}_3\text{N}_4/\text{Ca}_2\text{Nb}_2\text{TaO}_{10}$  nanosheet (80:20), (d)  $g\text{-C}_3\text{N}_4/\text{Ca}_2\text{Nb}_2\text{TaO}_{10}$  bulk (80:20) and (e)  $\text{Ca}_2\text{Nb}_2\text{TaO}_{10}$  nanosheets. Experimental conditions: 50 mg of photocatalyst with 1.0 wt% Pt as the cocatalyst, 200 ml of 10 vol% triethanolamine (TEOA) aqueous solution, 300 W xenon lamp equipped with 400 nm cut-off filter irradiation. (B). Photoluminescence spectra of  $g\text{-C}_3\text{N}_4$  bulk,  $g\text{-C}_3\text{N}_4$  nanosheets, and  $g\text{-C}_3\text{N}_4/\text{Ca}_2\text{Nb}_2\text{TaO}_{10}$  composites at an excitation wavelength of 325 nm: (a)  $g\text{-C}_3\text{N}_4$  bulk, (b)  $g\text{-C}_3\text{N}_4/\text{Ca}_2\text{Nb}_2\text{TaO}_{10}$  bulk composite (80:20), (c)  $g\text{-C}_3\text{N}_4$  nanosheets, (d)  $g\text{-C}_3\text{N}_4/\text{Ca}_2\text{Nb}_2\text{TaO}_{10}$  nanosheet composite (80:20), and (e)  $\text{Ca}_2\text{Nb}_2\text{TaO}_{10}$  nanosheets.

the UV/Vis spectrum edge of  $g\text{-C}_3\text{N}_4$  nanosheets exhibited a blue shift (by 0.1 eV) compared to its counterpart  $g\text{-C}_3\text{N}_4$  bulk sample. The increase in the band gap is attributed to the quantum confinement effect which could increase the ability of redox potential of generated charges on  $g\text{-C}_3\text{N}_4$  nanosheets [23,26]. The enhancement of photocatalytic  $\text{H}_2$  evolution of  $g\text{-C}_3\text{N}_4$  nanosheets could be attributable to the synergistic effect of the very small thickness (Fig. 3c) and large surface areas in the restacked nanosheet composites with increased reactive sites [22,26], which will be further supported by photoluminescence study in the following section.

When  $g\text{-C}_3\text{N}_4$  nanosheets were combined with  $\text{Ca}_2\text{Nb}_2\text{TaO}_{10}$  nanosheets (Fig. 5A,c), the  $g\text{-C}_3\text{N}_4/\text{Ca}_2\text{Nb}_2\text{TaO}_{10}$  nanosheet composites with an optimized mass ratio of 80: 20 shows drastically

enhanced photocatalytic  $\text{H}_2$  evolution to  $43.54 \mu\text{mol/h}$ . In order to investigate the cause of photocatalytic performance improvement of  $g\text{-C}_3\text{N}_4/\text{Ca}_2\text{Nb}_2\text{TaO}_{10}$  nanosheets, the  $g\text{-C}_3\text{N}_4/\text{Ca}_2\text{Nb}_2\text{TaO}_{10}$  bulk composite photocatalytic activity was tested. The photocatalytic activity of  $g\text{-C}_3\text{N}_4/\text{Ca}_2\text{Nb}_2\text{TaO}_{10}$  bulk composite was performed as shown in Fig. 5A(d). The  $g\text{-C}_3\text{N}_4/\text{Ca}_2\text{Nb}_2\text{TaO}_{10}$  bulk composite demonstrates  $\text{H}_2$  evolution rate of  $16.09 \mu\text{mol/h}$ , which is slightly higher than that of the pure  $g\text{-C}_3\text{N}_4$  bulk while its performance is far lower than that of the pure  $g\text{-C}_3\text{N}_4$  nanosheets and the  $g\text{-C}_3\text{N}_4/\text{Ca}_2\text{Nb}_2\text{TaO}_{10}$  nanosheet composite. In addition, we investigated the electron-hole pair recombination for  $g\text{-C}_3\text{N}_4$  bulk,  $g\text{-C}_3\text{N}_4$  nanosheets,  $\text{Ca}_2\text{Nb}_2\text{TaO}_{10}$  nanosheets, and  $g\text{-C}_3\text{N}_4/\text{Ca}_2\text{Nb}_2\text{TaO}_{10}$  composites via the photoluminescence (PL). The PL emission peak

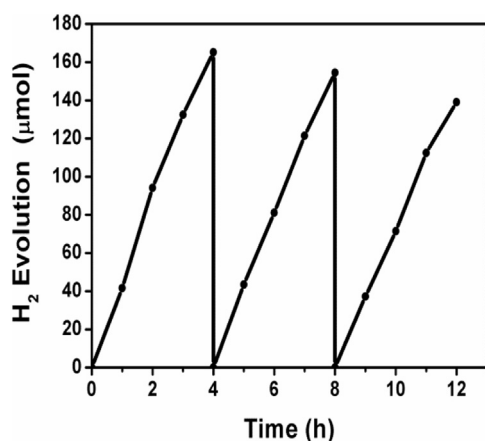


**Fig. 6.** Time course of H<sub>2</sub> evolution for 12 h with intermittent evacuation every 4 h in the presence of g-C<sub>3</sub>N<sub>4</sub>/Ca<sub>2</sub>Nb<sub>2</sub>TaO<sub>10</sub> nanosheet composite with a mass ratio of 80:20. Experiment conditions: 50 mg of photocatalyst with 1.0 wt% Pt as the co-catalyst, 200 ml of 10 vol% TEOA aqueous solution, 300 W xenon lamp equipped with 400 nm cut-off filter irradiation.

is correlated to electron-hole recombination within the photocatalysts. The higher the emission intensity corresponds to the severer recombination of electron-hole pairs [10]. Fig. 5B shows the PL spectra of the g-C<sub>3</sub>N<sub>4</sub>, Ca<sub>2</sub>Nb<sub>2</sub>TaO<sub>10</sub>, and g-C<sub>3</sub>N<sub>4</sub>/Ca<sub>2</sub>Nb<sub>2</sub>TaO<sub>10</sub> nanosheet composites. The broad emission peaks at about 460 nm resulted from excitation of g-C<sub>3</sub>N<sub>4</sub> at 325 nm [31]. The drastically quenched PL intensity was observed after g-C<sub>3</sub>N<sub>4</sub> bulk was exfoliated to g-C<sub>3</sub>N<sub>4</sub> nanosheets implying that the photogenerated electrons-holes have better separation in the nanosheets. This phenomenon confirms the synergistic effect of shortened electron diffusion distances [27] and the large surface area in the thin nanosheets [18]. After the addition of Ca<sub>2</sub>Nb<sub>2</sub>TaO<sub>10</sub> nanosheets, the PL intensity still substantially quenched, implying that efficient charge transfer between g-C<sub>3</sub>N<sub>4</sub> and Ca<sub>2</sub>Nb<sub>2</sub>TaO<sub>10</sub>. In Fig. 5B(b), the g-C<sub>3</sub>N<sub>4</sub>/Ca<sub>2</sub>Nb<sub>2</sub>TaO<sub>10</sub> bulk composite shows higher PL intensity than that of the g-C<sub>3</sub>N<sub>4</sub>/Ca<sub>2</sub>Nb<sub>2</sub>TaO<sub>10</sub> nanosheet composite, suggesting that the bulk composite has a much higher electron-hole recombination rate. In Fig. 5B(e), the Ca<sub>2</sub>Nb<sub>2</sub>TaO<sub>10</sub> nanosheet shows no signal under an excitation wavelength of g-C<sub>3</sub>N<sub>4</sub> (325 nm). Furthermore, the specific surface area of g-C<sub>3</sub>N<sub>4</sub>/Ca<sub>2</sub>Nb<sub>2</sub>TaO<sub>10</sub> nanosheet composite shows much higher (96.81 m<sup>2</sup>/g) than that of g-C<sub>3</sub>N<sub>4</sub>/Ca<sub>2</sub>Nb<sub>2</sub>TaO<sub>10</sub> bulk composite (8.59 m<sup>2</sup>/g). These results imply that synergistic properties of the increased surface area and composite heterojunction (Fig. 4(c, d)) can remarkably facilitate efficient charge carrier separation and migration of the composite photocatalyst, leading to improved photocatalytic hydrogen evolution in the composites.

The photocatalytic stability of g-C<sub>3</sub>N<sub>4</sub>/Ca<sub>2</sub>Nb<sub>2</sub>TaO<sub>10</sub> nanosheet composite with a mass ratio of 80:20 was investigated by proceeding the reaction for 12 h under irradiation with intermittent evacuation every 4 h and substitution of fresh sacrificial reagent solution. As shown in Fig. 6, the composite nanosheet can generate H<sub>2</sub> after 12 h with a total amount of 119.44 μmol with no apparent decrease observed. However, it can be noticed that the H<sub>2</sub> evolution was slightly decreased in the second and third cycles.

A possible mechanism is proposed for the enhancement of H<sub>2</sub> evolution activity of g-C<sub>3</sub>N<sub>4</sub>/Ca<sub>2</sub>Nb<sub>2</sub>TaO<sub>10</sub> nanosheet as shown schematically in Fig. 7. The conduction band and valence band potentials of g-C<sub>3</sub>N<sub>4</sub> are at −0.94 eV and −1.83 eV vs. NHE, respectively [26]. The conduction band edge of Ca<sub>2</sub>Nb<sub>2</sub>TaO<sub>10</sub> was referred to the value reported [32]. Metal oxides containing transition metal cations d 0 (i.e. Nb<sup>5+</sup>, Ta<sup>5+</sup>) and oxygen 2p orbitals has the valence band located at around 3 eV vs the normal hydrogen electrode (NHE; at pH 0). The as-synthesized Ca<sub>2</sub>Nb<sub>2</sub>TaO<sub>10</sub> exhibits

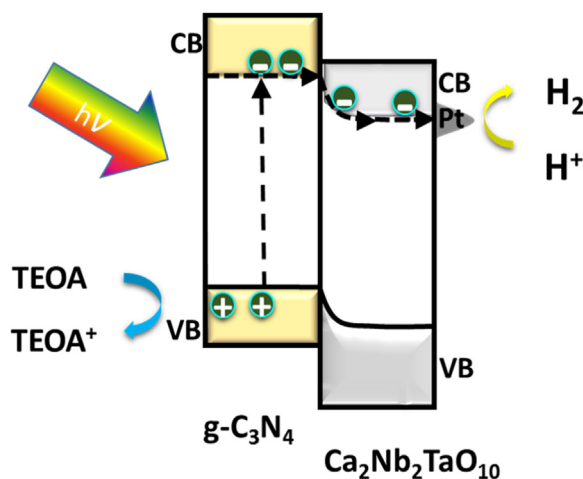


**Fig. 7.** Schematic diagram of the photoexcited charges separation and migration in g-C<sub>3</sub>N<sub>4</sub>/Ca<sub>2</sub>Nb<sub>2</sub>TaO<sub>10</sub> nanosheet composite under visible light irradiation.

a band gap of 3.67 eV estimated from the onset wavelength of the UV/Vis diffuse reflectance spectra (Fig. 2) and this is consistent with the previous report. [17]. Based on the valence band position and the optical band-gap, the conduction band level of around −0.67 eV is estimated for the Ca<sub>2</sub>Nb<sub>2</sub>TaO<sub>10</sub>. Since the conduction band potential of g-C<sub>3</sub>N<sub>4</sub> (−0.94 eV) is more negative than Ca<sub>2</sub>Nb<sub>2</sub>TaO<sub>10</sub> (−0.67 eV), the photoexcited electrons on g-C<sub>3</sub>N<sub>4</sub> can transfer easily to the Ca<sub>2</sub>Nb<sub>2</sub>TaO<sub>10</sub> via the interfacial contact and then to the co-catalyst Pt for H<sub>2</sub> evolution and the positive holes in the valence of g-C<sub>3</sub>N<sub>4</sub> can oxidize the sacrificial reagent (TEOA). Hence, the heterostructured photocatalyst can efficiently transfer photoinduced charge carriers and suppress the electron-hole recombination.

#### 4. Conclusions

In summary, we reported a new type of two-dimensional composites by combining exfoliated g-C<sub>3</sub>N<sub>4</sub> nanosheets and Ca<sub>2</sub>Nb<sub>2</sub>TaO<sub>10</sub> nanosheets via a facile solution exfoliation-reassembly process. The resultant g-C<sub>3</sub>N<sub>4</sub>/Ca<sub>2</sub>Nb<sub>2</sub>TaO<sub>10</sub> nanosheet composites exhibited intimate interfacial contact, leading to enhanced photogenerated charge separations in the photocatalytic reactions. We further applied the g-C<sub>3</sub>N<sub>4</sub>/Ca<sub>2</sub>Nb<sub>2</sub>TaO<sub>10</sub> nanosheet composites as the photocatalysts in hydrogen evolution under visible-light illumination. The g-C<sub>3</sub>N<sub>4</sub>/Ca<sub>2</sub>Nb<sub>2</sub>TaO<sub>10</sub> nanosheet composite with the 80:20 ratio shows the best photocatalytic performance for H<sub>2</sub> production (43.54 μmol/h), around 2.8 times higher than that of the individual g-C<sub>3</sub>N<sub>4</sub> bulk. The conduction band difference in the g-C<sub>3</sub>N<sub>4</sub>/Ca<sub>2</sub>Nb<sub>2</sub>TaO<sub>10</sub> heterojunction facilitates the photoexcited charges transfer and simultaneously suppresses charge recombination, which in turn markedly improves its photocatalytic performance. The present work provides an effective strategy to design new semiconductor photocatalysts based on two-dimensional nanosheet heterojunction for solar hydrogen evolution.

#### Acknowledgements

The authors would like to acknowledge the financial support from Australian Research Council through its DP and FF programs. This work was performed in part at the Queensland node of the Australian National Fabrication Facility. S.T. would like to acknowledge the support from the Royal Thai Government Scholarship, Ministry of Science and Technology.



## References

- [1] S.J.A. Moniz, et al., Visible-light driven heterojunction photocatalysts for water splitting – a critical review, *Energy Environ. Sci.* 8 (3) (2015) 731–759.
- [2] R. Abe, Recent progress on photocatalytic and photoelectrochemical water splitting under visible light irradiation, *J. Photochem. Photobiol. C: Photochem. Rev.* 11 (4) (2010) 179–209.
- [3] R.C. Pawar, V. Khare, C.S. Lee, Hybrid photocatalysts using graphitic carbon nitride/cadmium sulfide/reduced graphene oxide (g-C<sub>3</sub>N<sub>4</sub>/CdS/RGO) for superior photodegradation of organic pollutants under UV and visible light, *Dalton Trans.* 43 (33) (2014) 12514–12527.
- [4] Z. Xing, et al., A new type of carbon nitride-based polymer composite for enhanced photocatalytic hydrogen production, *Chem. Commun.* 50 (51) (2014) 6762–6764.
- [5] J.S. Jang, H.G. Kim, J.S. Lee, Heterojunction semiconductors: a strategy to develop efficient photocatalytic materials for visible light water splitting, *Catal. Today* 185 (1) (2012) 270–277.
- [6] C. Tan, H. Zhang, Two-dimensional transition metal dichalcogenide nanosheet-based composites, *Chem. Soc. Rev.* 44 (9) (2015) 2713–2731.
- [7] I.Y. Kim, et al., UNique advantages of exfoliated 2D nanosheets for tailoring the functionalities of nanocomposites, *J. Phys. Chem. Lett.* 5 (23) (2014) 4149–4161.
- [8] J.L. Gunjakar, et al., Exploration of nanostructured functional materials based on hybridization of inorganic 2D nanosheets, *J. Phys. Chem. C* 118 (8) (2014) 3847–3863.
- [9] S. Yang, et al., Exfoliated graphitic carbon nitride nanosheets as efficient catalysts for hydrogen evolution under visible light, *Adv. Mater.* 25 (17) (2013) 2452–2456.
- [10] H. Shi, et al., Polymeric g-C<sub>3</sub>N<sub>4</sub> coupled with NaNbO<sub>3</sub> nanowires toward enhanced photocatalytic reduction of CO<sub>2</sub> into renewable fuel, *ACS Catal.* 4 (10) (2014) 3637–3643.
- [11] S. Fang, et al., Effect of acid on the photocatalytic degradation of rhodamine B over g-C<sub>3</sub>N<sub>4</sub>, *Appl. Surf. Sci.* 358 (Part A) (2015) 336–342.
- [12] M. Reza Gholipour, et al., Nanocomposite heterojunctions as sunlight-driven photocatalysts for hydrogen production from water splitting, *Nanoscale* 7 (18) (2015) 8187–8208.
- [13] Y. Hou, et al., Constructing 2D porous graphitic C<sub>3</sub>N<sub>4</sub> nanosheets/nitrogen-doped graphene/layered MoS<sub>2</sub> Ternary nanojunction with enhanced photoelectrochemical activity, *Adv. Mater.* 25 (43) (2013) 6291–6297.
- [14] J. Ran, et al., Porous P-doped graphitic carbon nitride nanosheets for synergistically enhanced visible-light photocatalytic H<sub>2</sub> production, *Energy Environ. Sci.* 8 (12) (2015) 3708–3717.
- [15] S. Fang, et al., Effect of carbon-dots modification on the structure and photocatalytic activity of g-C<sub>3</sub>N<sub>4</sub>, *Appl. Catal. B: Environ.* 185 (2016) 225–232.
- [16] Z.a. Huang, et al., Effect of contact interface between TiO<sub>2</sub> and g-C<sub>3</sub>N<sub>4</sub> on the photoreactivity of g-C<sub>3</sub>N<sub>4</sub>/TiO<sub>2</sub> photocatalyst: (0 0 1) vs (1 0 1) facets of TiO<sub>2</sub>, *Appl. Catal. B: Environ.* 164 (2015) 420–427.
- [17] K. Maeda, M. Eguchi, T. Oshima, Perovskite oxide nanosheets with tunable band-edge potentials and high photocatalytic hydrogen-evolution activity, *Angew. Chem. Int. Ed.* 53 (48) (2014) 13164–13168.
- [18] X. Lu, et al., Facile one step method realizing scalable production of g-C<sub>3</sub>N<sub>4</sub> nanosheets and study of their photocatalytic H<sub>2</sub> evolution activity, *J. Mater. Chem. A* 2 (44) (2014) 18924–18928.
- [19] M. Kakihana, et al., Polymerized complex synthesis of perovskite lead titanate at reduced temperatures: possible formation of heterometallic (Pb,Ti)-citric acid complex, *Chem. Mater.* 9 (2) (1997) 451–456.
- [20] S. Ikeda, et al., Preparation of K<sub>2</sub>La<sub>2</sub>Ti<sub>3</sub>O<sub>10</sub> by polymerized complex method and photocatalytic decomposition of water, *Chem. Mater.* 10 (1) (1998) 72–77.
- [21] X. Cai, et al., Tuning the surface charge of 2D oxide nanosheets and the bulk-scale production of superlatticelike composites, *J. Am. Chem. Soc.* 137 (8) (2015) 2844–2847.
- [22] Y. Lu, et al., Exfoliated carbon nitride nanosheets decorated with NiS as an efficient noble-metal-free visible-light-driven photocatalyst for hydrogen evolution, *Phys. Chem. Chem. Phys.* 17 (26) (2015) 17355–17361.
- [23] P. Niu, et al., Graphene-like carbon nitride nanosheets for improved photocatalytic activities, *Adv. Funct. Mater.* 22 (22) (2012) 4763–4770.
- [24] K. Maeda, M. Eguchi, Structural effects of two-dimensional perovskite Ca<sub>2</sub>Nb<sub>2</sub>TaO<sub>10</sub>- nanosheets for photocatalytic hydrogen evolution, *Catal. Sci. Technol.* 6 (4) (2016) 1064–1069.
- [25] B. Chai, et al., Graphitic carbon nitride (g-C<sub>3</sub>N<sub>4</sub>)-Pt-TiO<sub>2</sub> nanocomposite as an efficient photocatalyst for hydrogen production under visible light irradiation, *Phys. Chem. Chem. Phys.* 14 (48) (2012) 16745–16752.
- [26] Q. Lin, et al., Efficient synthesis of monolayer carbon nitride 2D nanosheet with tunable concentration and enhanced visible-light photocatalytic activities, *Appl. Catal. B: Environ.* 163 (2015) 135–142.
- [27] J. Tian, et al., Three-dimensional porous supramolecular architecture from ultrathin g-C<sub>3</sub>N<sub>4</sub> nanosheets and reduced graphene oxide: solution self-assembly construction and application as a highly efficient metal-free electrocatalyst for oxygen reduction reaction, *ACS Appl. Mater. Interfaces* 6 (2) (2014) 1011–1017.
- [28] Z. Xing, et al., Nanohybrid materials of titania nanosheets and plasmonic gold nanoparticles for effective hydrogen evolution, *Appl. Catal. A: Gen.* 521 (2016) 96–103.
- [29] D. Chen, et al., Nanospherical like reduced graphene oxide decorated TiO<sub>2</sub> nanoparticles: an advanced catalyst for the hydrogen evolution reaction, *Sci. Rep.* 6 (2016) 20335.
- [30] Y. Tian, et al., Hydrothermal synthesis of graphitic carbon nitride–Bi<sub>2</sub>WO<sub>6</sub> heterojunctions with enhanced visible light photocatalytic activities, *ACS Appl. Mater. Interfaces* 5 (15) (2013) 7079–7085.
- [31] L. Ge, et al., Synthesis and efficient visible light photocatalytic hydrogen evolution of polymeric g-C<sub>3</sub>N<sub>4</sub> coupled with cds quantum dots, *J. Phys. Chem. C* 116 (25) (2012) 13708–13714.
- [32] D.E. Scaife, Oxide semiconductors in photoelectrochemical conversion of solar energy, *Sol. Energy* 25 (1) (1980) 41–54.